

Investigation of de Haas–van Alphen and Shubnikov–de Haas quantum oscillations in PrTe₃Xiong Luo,^{1,*} Xiaoxuan Ma^{2,*}, Junchao Zhang,¹ Yu Xing,¹ Aoli Shen,¹ Haoran Ye,¹ Shengchun Shen,³ Jin Peng,¹ Shixun Cao², Shuai Dong,¹ and Linglong Li^{1,†}¹Key Laboratory of Quantum Materials and Devices of Ministry of Education, School of Physics, Southeast University, Nanjing 211189, China²Department of Physics, Materials Genome Institute, International Center for Quantum and Molecular Structures, Shanghai University, Shanghai 200444, China³Department of Physics, University of Science and Technology of China, Hefei 230026, China

(Received 14 September 2023; revised 23 November 2023; accepted 19 December 2023; published 11 January 2024)

The discovery of high mobility in quasi-two-dimensional (2D) rare-earth tritellurides has had a transformative impact on the field of quantum materials, particularly in relation to charge-density-wave phenomena. Despite significant progress, the complex electronic properties of these materials remain enigmatic, primarily due to a lack of comprehensive understanding regarding their transport characteristics. In this paper, we present a meticulous analysis of the magnetic-field-induced properties of PrTe₃ in both bulk and nanoflake forms. Our investigations unveil a diverse range of distinct frequencies exhibited by the observed quantum oscillation effect. By combining angular-dependent magnetoresistance with Shubnikov–de Haas quantum oscillations, we successfully fit the data to a $1/\cos(\theta)$ dependence model, providing compelling evidence for a 2D-like Fermi surface and underscoring the pronounced 2D nature of the Fermi surface pockets. Furthermore, our findings reveal a zero Berry phase, corroborating the Lifshitz-Onsager quantization rule. Notably, we report a remarkable magnetoresistance value of 1800% in the 60 nm device, coupled with an electron mobility of $4.1 \times 10^4 \text{ cm}^2 \text{ V}^{-1} \text{ s}^{-1}$. These exceptional outcomes are poised to stimulate heightened interest in exploring the potential of layered rare-earth tritellurides in the realm of quantum oscillation.

DOI: [10.1103/PhysRevB.109.035121](https://doi.org/10.1103/PhysRevB.109.035121)

I. INTRODUCTION

In the realm of fundamental condensed matter physics, the interactions between pairs of parameters often give rise to broken-symmetry ground states at specific temperatures. An illustrative example of this phenomenon is the formation of charge density waves (CDWs) in materials exhibiting highly anisotropic band structures. The CDW state can be described by a spatial modulation $\sim \cos(\mathbf{q} \cdot \mathbf{x} + \varphi)$. In ideal one-dimensional (1D) systems, the Fermi surface is composed of two points at Fermi wave vector places ($-k_F$ and $+k_F$) in reciprocal space. The CDW state primarily arises from a perfect Fermi surface nesting, characterized by the definition of a modulation wave vector $\mathbf{q} = 2k_F$. Thus, all 1D systems are subordinated to CDW transitions (also called Peierls transitions in this situation). However, in two-dimensional (2D) and three-dimensional (3D) compounds, the CDW state is driven by more intricate mechanisms [1,2], and only certain parts of the Fermi surface are subject to good nesting, leading to an incommensurate nesting of the Fermi surface below the CDW transition temperature while retaining metallic behavior. In multiband systems, this can lead to the suppression of charge scattering, consequently resulting in enhanced charge mobility [3].

The CDW state has been extensively studied due to its significant impact on the electronic properties of materials. Experimental and theoretical investigations have revealed a rich variety of CDW phenomena in diverse materials, ranging from low-dimensional systems to complex intermetallic compounds [4–9]. Among them, the quasi-2D rare-earth tritelluride ($R\text{Te}_3$) family has garnered considerable attention in recent decades due to its intriguing properties encompassing CDW transitions, magnetism, and superconductivity [10–13]. The interplay between the CDW order and other degrees of freedom, such as spin and lattice, further enhances the complexity of the CDW phenomenon in $R\text{Te}_3$. Particularly noteworthy is its exceptional charge mobility, which surpasses that of all known magnetic materials [10,12–19], which may be attributed to the steep conduction bands resulting from the square net and the enhancement of scattering time because of partial gap opening of the Fermi surface [17]. The $R\text{Te}_3$ family of compounds demonstrates a remarkable lattice modulation characterized by an incommensurate wave vector $\mathbf{q}_1 = 2/7\mathbf{c}^*$ ($\mathbf{c}^* = 2\pi/c$). The Peierls transition temperature within this family varies, ranging from 244 K in TmTe_3 to >450 K in LaTe_3 , with higher transition temperatures associated with a larger lattice constant. Notably, in heavy rare-earth members ($R = \text{Tb}, \text{Dy}, \text{Ho}, \text{Er}, \text{Tm}$), a secondary CDW transition occurs, accompanied by an additional wave vector $\mathbf{q}_2 = 1/3\mathbf{a}^*$ ($\mathbf{a}^* = 2\pi/a$), which was observed by DiMasi *et al.* [20] through transmission electron microscopy (TEM). However, the CDW temperature corresponding to this second transition is significantly lower than that of the primary transition and

*These authors contributed equally to this work.

†linglongli@seu.edu.cn

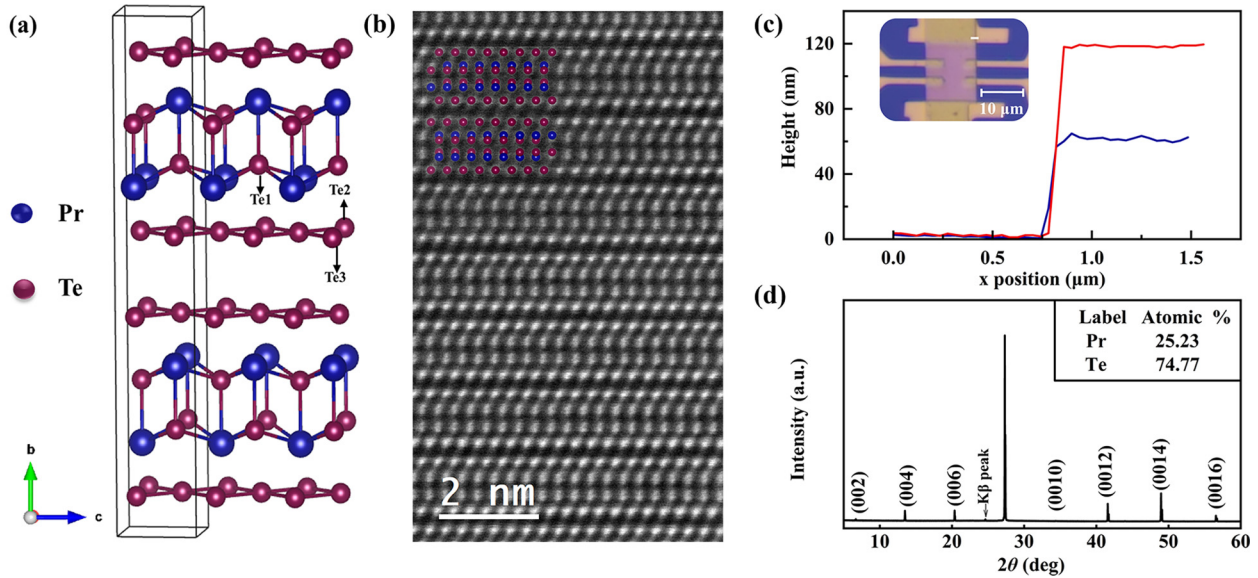


FIG. 1. (a) Crystal structure of PrTe₃, illustrating the arrangement of atoms within the lattice. (b) High-angle annular dark-field (HAADF)-scanning transmission electron microscopy (STEM) images of PrTe₃. (c) Cross-sectional profiles of atomic force microscopy (AFM) morphology, demonstrating the thickness of 60 and 120 nm nanoflakes. The inset is an optical image of a 60 nm nanoflake. (d) X-ray diffraction pattern of a PrTe₃ single crystal, with the inset presenting the atomic composition ratio of Pr/Te $\approx \frac{1}{3}$, obtained from energy-dispersive x-ray spectroscopy (EDX) analysis.

exhibits an inverse relationship with the lattice constant [21]. Comprehending the underlying mechanisms and properties of CDWs is crucial for advancing our understanding of fundamental condensed matter physics and exploring potential applications in fields such as electronics and energy storage [22–25].

PrTe₃, a member of the rare-earth tritellurides, possesses a weakly orthorhombic structure with *Cmcm* space group. Its crystal arrangement comprises Pr-Te slabs separated by two tellurium layers, wherein the long *b* axis is perpendicular to the Te planes, as shown in Fig. 1(a). van der Waals interactions govern the interconnection between the Te layers, enabling the layered nature and facilitating the exfoliation of thin nanoflakes from bulk crystals. For PrTe₃, its CDW temperature is still unknown. Lee *et al.* [26] and Seong *et al.* [27] have explored the electronic structure of the CDW state. Nonetheless, there remains a considerable dearth of knowledge concerning the low-temperature magnetotransport properties of PrTe₃. In this paper, we elucidate the fermiology and low-temperature transport properties of rare-earth praseodymium tritelluride (PrTe₃). Our investigations encompass the analysis of both the de Haas–van Alphen (dHvA) and Shubnikov–de Haas (SdH) effects in bulk and/or nanoflakes. The angular-dependent magnetoresistance (AMR) and SdH oscillation definitively establish the 2D nature of the Fermi surface, while the application of the Lifshitz-Onsager quantization rule provides valuable insight into the band dispersion. Notably, our results unveil an extraordinary longitudinal magnetoresistance (MR) of 1800% at 2 K and 11 T in the 60 nm nanodevice. Additionally, we evaluate the electron mobility (μ_e) and hole mobility (μ_h) at 2 K, yielding values of 4.1×10^4 and 9×10^3 cm² V⁻¹ s⁻¹, respectively, underscoring the potential of PrTe₃ for high-mobility device application.

II. EXPERIMENTAL DETAILS

Single crystals of PrTe₃ were synthesized utilizing a self-flux method, following the procedure outlined elsewhere [10]. Te (Aladdin, 99.99%) and Pr (Aladdin, 99.9%) were accurately weighed in a ratio of 97:3 and thoroughly mixed. Subsequently, the resulting raw materials were hermetically sealed within an evacuated quartz ampoule and subjected to a temperature of 900°C for a duration of 12 h, followed by a controlled cooling at a rate of 2°C/min to reach 550°C. Nanoflake samples were obtained using the mechanical exfoliation method employing scotch tape. Afterward, the nanoflakes were transferred onto prepatterned Hall bar electrodes (fabricated via standard electron beam lithography, 50 nm Au with 5 nm Ni buffer layer deposited using thermal evaporation) on 300 nm SiO₂/Si substrates within an argon-protected glovebox. The thickness of the nanoflakes was determined using atomic force microscopy (Dimension ICON). For structure analysis of the bulk sample, an x-ray diffractometer (SmartLab-3, Rigaku Corp.) was employed. Additionally, the chemical composition of the PrTe₃ crystal was analyzed through energy dispersive x-ray spectroscopy (FEI Inspect F50). The TEM specimens were prepared by focused ion beam (FIB, Helios 4, FEI) milling. At the final stage of FIB milling, a low-energy Ga⁺ ion beam at 2 kV was used to reduce the beam damage. Scanning transmission electron microscopy (STEM) images were taken by a field emission (S)TEM (Thermo Scientific Spectra 300) equipped with double Cs correctors operated at 300 kV. Temperature- and field-dependent dc magnetization measurements were carried out using a Quantum Design PPMS equipped with the vibrating sample magnetometer option. All magnetotransport measurements were performed in a 12 T Teslatron PT magnet (Oxford Instruments) employing a custom-made probe

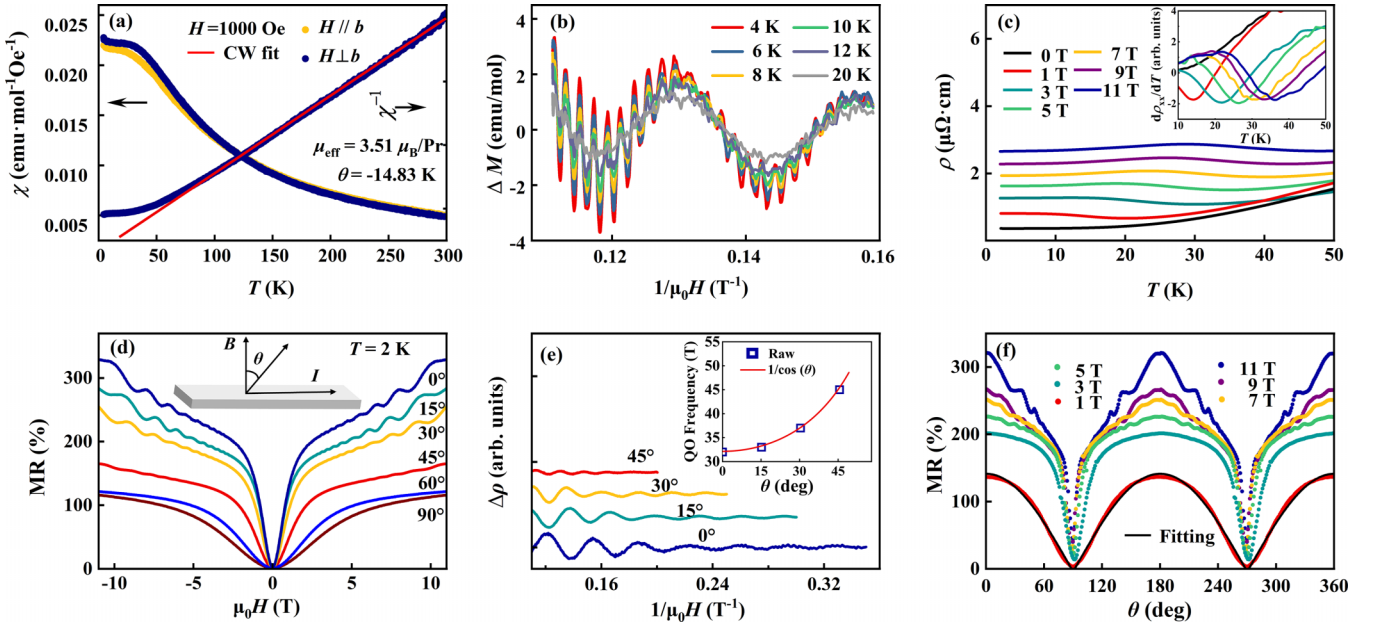


FIG. 2. (a) Temperature-dependent dc magnetization of bulk PrTe_3 under an applied magnetic field of 1000 Oe. A Curie-Weiss fitting is conducted using the zero-field-cooled curve within the temperature range of 250–300 K. (b) de Haas–van Alphen (dHvA) oscillatory components ΔM at various temperatures obtained by subtracting a smooth background with the magnetic field parallel to the crystallographic b axis ($\mu_0 H // b$ axis). (c) Resistivity-temperature (R vs T) curves of the bulk sample measured at different magnetic fields < 50 K. (d) Angular dependence of the magnetoresistance (MR) of the bulk sample at 2 K. (e) Angular dependence of the α Shubnikov–de Haas (SdH) oscillation, with the inset showing $1/\cos(\theta)$ fit of the α frequency at different angles θ . (f) Angular dependence of longitudinal MR in the bulk sample measured at 2 K under various magnetic fields. The black line represents the fit using the two-dimensional (2D) model of $|\cos(\theta)|$.

coupled with an SR830 lock-in amplifier (Stanford Research Systems).

III. RESULTS AND DISCUSSIONS

The high-angle annular dark-field (HAADF) aberration-corrected STEM images of the single crystal, as depicted in Fig. 1(b), reveal the precise stacking arrangement of Pr-Te and Te planes, which corresponds to the expected lattice structure of PrTe_3 . This observation confirms the exceptional crystalline quality exhibited by the single crystal. Nanoflakes with thicknesses of 60 and 120 nm were prepared by the mechanical exfoliation method and then transferred onto the substrates. The thicknesses of the devices were confirmed by the cross-sectional profiles of the morphology from atomic force microscopic scanning, as shown in Fig. 1(c), and the corresponding optical image is provided in Fig. 1(c). To determine the crystalline structure and stoichiometric ratio, x-ray diffraction (XRD) patterns and energy dispersive x-ray detector (EDX) spectra were acquired, as shown in Fig. 1(d). The crystalline structure is confirmed by the XRD results, revealing distinct $(00l)$ peaks with minimal impurity signals. The stoichiometric ratio of Pr : Te was determined to be 1:2.96 by the EDX analysis, which closely approximates the nominal value of 1:3, indicating the accurate composition of the crystal.

Subsequently, magnetic characterizations were performed on the crystals. Figure 2(a) presents the temperature-dependent dc magnetization (M vs T) of the bulk sample, recorded across the temperature range of 300–4 K under a magnetic field of 1000 Oe, with measurements conducted in

both in-plane and out-of-plane directions, i.e., parallel and perpendicular to the b axis, as indicated by the labels in Fig. 2(a), respectively. The magnetization increases as the temperature decreases and stabilizes < 25 K. Even at a significantly higher cooling field of 14 T, as shown in Fig. S1(a) in Supplemental Material [28], negligible changes were observed in the M vs T curves, consistent with previous reports [10]. The magnetic susceptibility in the high-temperature range (> 200 K) follows the Curie-Weiss law (zero-field cooling), and the temperature-independent contribution to the susceptibility was ignored. The Weiss temperature (θ) was determined to be -11.83 K. Furthermore, the effective moment of the Pr ion was calculated to be $3.51 \mu_B/\text{f.u.}$, a value comparable with the theoretical prediction of $3.58 \mu_B$ for Pr^{3+} [29,30], thus suggesting that the magnetic moments are localized below the Fermi level. Consequently, it is noteworthy that no long-range magnetic ordering was observed within the entire temperature range covered by the M vs T measurement. The observed phenomena are a consequence of the impact of the crystal field on the non-Kramers ions with a $4f^2$ configuration in PrTe_3 , leading to the formation of a singlet state at low temperatures, which is characteristic of Van Vleck paramagnetism. Similar phenomena have been observed in PrSb [31] and $\text{PrPt}_4\text{Ge}_{12}$ [32], where the Pr^{3+} ninefold degenerate $J = 4$ multiplet split into a singlet Γ_1 , a doublet Γ_{23} , and two triplets Γ_4 [33].

Magnetic susceptibility is commonly employed to investigate the Fermi surface of metals using the principle of Landau quantization of fermions in the presence of a strong magnetic field, known as the dHvA effect. The magnetic field dependence of magnetization along the $\mu_0 H // b$ axis and $\mu_0 H // ac$

plane at different temperatures is illustrated in Figs. S1(b) and S1(c) in the Supplemental Material [28], respectively. After subtracting a third-order polynomial background (over the field range 5–9 T) of the dataset along $\mu_0 H // b$ axis, the relationship between ΔM and the inverse field $1/\mu_0 H$ at various temperatures is carried out as shown in Fig. 2(b). Notably, the curves exhibit distinct oscillation modes characterized by varying frequencies. As the temperature increases from 4 to 20 K, the oscillation peaks progressively decrease in intensity. For the transport properties of bulk PrTe₃ samples, the temperature-dependent resistivity of bulk and nanoflakes was carried out, as shown in Fig. S2 in the Supplemental Material [28], and the resistivity at room temperature of the three samples is $\sim 20 \mu\Omega \text{ cm}$. The residual resistance ratio (RRR) for bulk, 120 nm, and 60 nm nanoflake samples, within the temperature range of 300–2 K, was found to be 47, 163, and 297, respectively. The thickness-dependent RRR values may be influenced by the crystalline quality of the specimens. Thinner flakes exhibit fewer defects and unanticipated boundaries, resulting in reduced carrier scattering and larger RRR values of these samples. Below CDW transition temperature, these samples exhibit characteristic metallic behavior in the absence of an applied magnetic field. This behavior can be ascribed to the imperfect nesting of the Fermi surface [21]. To gain insight into the influence of the magnetic field on the electronic state, the temperature dependence of the resistivity was measured from 2 to 50 K at the different fields with $\theta = 0^\circ$, where θ is the angle between the b axis and the magnetic field, as depicted in Fig. 2(c). A distinct humplike feature was observed, shifting to the higher-temperature regions with increasing magnetic field. The derivative of $\rho_{xx}(T)$ at different fields, as shown in the inset of Fig. 2(c), further confirms such behavior. The dips move to the higher-temperature region with increasing magnetic field. Such phenomena have been reported in LaTe₃ and NdTe₃ [18,19], which are like the second CDW transition observed in heavy rare-earth RTe₃ systems [21,27]. According to the calculations by Pariari *et al.* [18], this phenomenon may be related to the field-induced CDW transition, and further experimental works can be focused on STM measurement under low-temperature and high-magnetic-field circumstances.

To investigate the Fermi surface structure of PrTe₃, we carried out electrical transport measurements at low temperatures using the same sample. The SdH effect is manifested in the MR at different temperatures with $\mu_0 H // b$ axis, where MR is defined as $[\rho(\mu_0 H) - \rho(0)]/\rho(0) \times 100\%$. We performed MR measurements up to $\mu_0 H = 11$ T for the temperature range of 2–50 K, as shown in Fig. S3 in the Supplemental Material [28]. Figure 2(d) exhibits the angular-dependent MR at 2 K [28]. As we measured the MR at various θ values ranging from 0° to 90° , we observed a gradual decrease in the maximum relative MR at 11 T, accompanied by a weakening of the MR oscillations. To gain deeper insight into the Fermi surface structure, we performed fast Fourier transformation (FFT) on the SdH oscillation α frequencies of the data collected from 3 to 11 T, the results are shown in Fig. 2(e). The observed frequencies increase with rising θ and follow a $1/\cos(\theta)$ relationship, providing compelling evidence for a 2D Fermi surface origin. Additionally, the angular-dependent MR results in Fig. 2(f) corroborate the 2D Fermi surface, exhibiting

a twofold symmetry proportional to $|\cos(\theta)|$, which is consistent with previous angle-resolved photoemission spectroscopy (ARPES) findings [26].

The quantum oscillation observed in PrTe₃ can be described by the Lifshitz-Kosevich (L-K) formula [20,21]:

$$\Delta M \propto -\frac{\lambda T}{\sin(\lambda T)} \exp(-\lambda T_D) \sin \left[2\pi \left(\frac{F}{B} + \gamma - \delta \right) \right], \quad (1)$$

$$\Delta \rho \propto \frac{\lambda T}{\sin(\lambda T)} \exp(-\lambda T_D) \cos \left[2\pi \left(\frac{F}{B} + \gamma - \delta \right) \right]. \quad (2)$$

The amplitude of temperature-dependent quantum oscillations can be defined by the thermal damping factor, as defined in Eq. (3):

$$R_T = \frac{\lambda T}{\sinh(\lambda T)}. \quad (3)$$

Here, λ is given by $\lambda = 2\pi^2 k_B m^* / \hbar e B$, where k_B represents the Boltzmann constant, \hbar denotes the reduced Planck's constant, m^* corresponds to the effective mass, and $2\pi^2 k_B / \hbar e$ is equal to 14.69 T/K. The parameter T_D is the Dingle temperature. The oscillation frequency is denoted by F , and the phase factor $\gamma - \delta$ is involved, with γ defined as $\gamma = \frac{1}{2} - \frac{\Phi_B}{2\pi}$. The Berry phase Φ_B is associated with the oscillation phase, and δ is a phase offset that depends on the dimensionality of the Fermi surface. In the case of a 2D surface, δ is set to 0, whereas for a 3D surface, it takes values of $\pm \frac{1}{8}$. To understand the magnetic characterization results further, the FFT analysis of the dHvA oscillation was conducted, and the results are shown in the inset of Fig. 3(a), revealing five oscillation frequencies [$F(\alpha) = 37$ T, $F(\beta_1) = 470$ T, $F(\beta_2) = 521$ T, $F(\gamma_1) = 836$ T, and $F(\gamma_2) = 877$ T] resolved for the magnetic field oriented parallel to the b axis at 4 K. This suggests the presence of multiple Fermi surface pockets with significant cross-section areas. In the RTe₃ family, the interaction between the p_x and p_z orbitals of Te square leads to an inner square Fermi surface inside the first Brillouin zone (BZ) and four outer pockets in the BZ boundary. Additionally, the unit cell size of the crystal exceeds that of the Te sheet, resulting in a reduced BZ and a backfolding of the Fermi surface into the smaller BZ [15,18]. According to previous ARPES research, the α frequency in quantum oscillation may be assigned to the wings of the butterfly structure near the X point, which is responsible for the high mobility in this system. The $\beta_{1,2}$ and $\gamma_{1,2}$ frequencies are linked to the pockets around the X point and can be attributed to the bilayer splitting along k_y . Notably, these frequencies remain unaffected by the CDW transition, as indicated in previous studies [15,17]. The temperature dependence of the dHvA oscillation amplitude is plotted in Fig. 3(b) and effectively fitted using the thermal damping factor described in Eq. (3). The solid line represents the fitting results obtained using the L-K formula, yielding effective masses (m^*). The effective mass (m^*) of the α pocket is measured to be $0.061 m_e$, while the β_1 and β_2 pockets exhibit lower oscillation amplitudes and larger effective masses compared to the α pocket.

The layered nature of RTe₃ presents an opportunity to explore the potential enhancement of SdH oscillations in nanoflakes [11]. Utilizing a mechanical exfoliation approach,

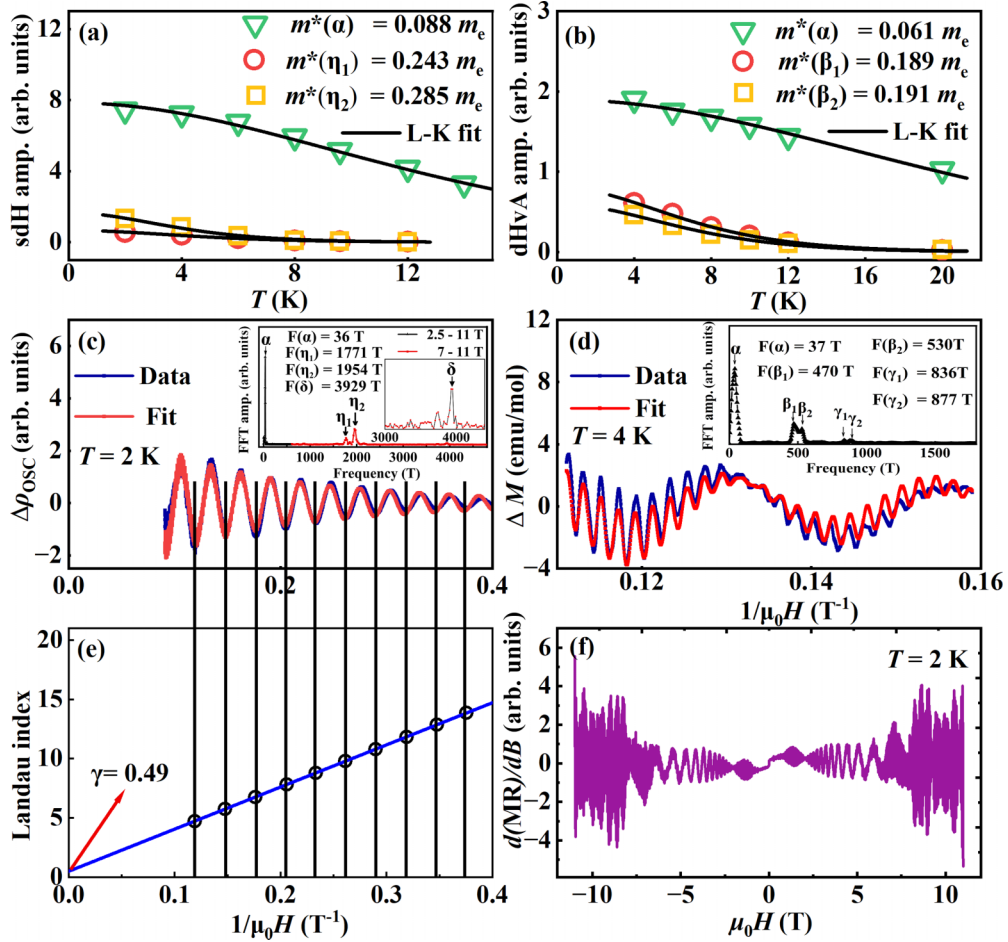


FIG. 3. (a) de Haas–van Alphen (dHvA) oscillations in the magnetization at 4 K. The inset shows the fast Fourier transformation (FFT) analysis. (b) Temperature-dependent amplitudes of α , β_1 , and β_2 oscillations at a magnetic field of 7.6 T, obtained from dHvA measurements. The solid lines represent fits using the Lifshitz-Kosevich (L-K) formula. (c) Shubnikov–de Haas (SdH) oscillations in resistivity, obtained by subtracting the polynomial background of magnetoresistance (MR) for a 60 nm sample. The inset shows the FFT of the oscillation, with the α frequency determined in the range of 2.5–11 T, and η_1 and η_2 resolved within the magnetic field range of 7–11 T. (d) Temperature dependence of the amplitudes of the α , η_1 , and η_2 oscillations at a magnetic field of 7.6 T, observed via SdH oscillations. The solid lines correspond to fits using the L-K formula. (e) Landau index plotted against $1/B$, obtained from the valley positions of the SdH oscillations. The solid line shows a linear fit, yielding a residual Landau index of $n = 0.49$. (f) First-order derivative of MR as a function of $\mu_0 H$ at 2 K.

we fabricated nanodevices of PrTe_3 with thicknesses of 60 and 120 nm in an argon-protected atmosphere. To prevent surface oxidation, the devices were quickly transferred to a magnet within 5 min. To determine accurate fitting parameters, we first extract the oscillation frequency by performing FFT, which allows us to obtain the individual amplitudes at different temperatures, as shown in Fig. 3(c). Subsequently, we fit the temperature dependence of the oscillation amplitude using the thermal damping factor, enabling us to extract the effective mass m^* . By applying FFT analysis to the sdH data, we identified three additional frequencies emerging at the higher magnetic field: $F(\eta_1) = 1771$ T, $F(\eta_2) = 1954$ T, and $F(\delta_1) = 3929$ T, where η and δ correspond to closed contours around the X point and closed contour of the inner part of the Fermi surface, respectively. These frequencies may be the result of the reconstruction of the Fermi surface caused by CDW [17,19,24]. With the obtained effective mass, we can then use the L-K formula to reveal the Dingle temperature. Finally, the quantum lifetime τ_q and mobility μq are determined

by using $T_D = \hbar/2\pi k_B \tau_q$ and $\mu q = e\hbar/2\pi k_B m^* T_D$. A similar trend is observed in the SdH oscillation; the results are shown in Fig. 3(d), where the L-K fitting yields larger effective mass values for the η_1 and η_2 pockets, and a lower effective mass ($m^* = 0.088 m_e$) for the α pocket of the SdH oscillation, the corresponding fitting of ΔM and $\Delta \rho$ vs $1/\mu_0 H^{-1}$ are given in Figs. 3(c) and 3(d) as the solid blue curves. We also measure the M vs H curve of PrTe_3 up to 14 T magnetic field; the fitting curve is given in Fig. S4 in the Supplemental Material [28]. To analyze the data further, we applied the Lifshitz-Onsager quantization rule: $F/B + \gamma - \delta = n$, where n represents the Landau index. The Landau index vs $1/B$ plot is shown in Fig. 3(e). Notably, the Landau level index corresponds to the valley positions of the SdH oscillations, marked by vertical lines in Figs. 3(c) and 3(e). Through linear fitting, the residual Landau index is determined to be 0.49, indicating a zero Berry phase [34]. Consequently, the calculated mobility reaches up to $5.73 \times 10^3 \text{ cm}^2 \text{ V}^{-1} \text{ s}^{-1}$, with more detailed values listed in Table I. By performing quantum oscillation measurements,

TABLE I. Parameters from L-K fit in both dHvA and SdH quantum oscillations at 4 and 2 K, respectively. NA = not applicable.

Method	Sample geometry	Pocket	F (T)	$m^* (m_e)$	T_D (K)	μ_q (cm ² /V S)
dHvA	Bulk	α	37	0.061	6.2	5.65×10^3
		β_1	470	0.189	4.2	2.69×10^3
		β_2	530	0.191	5.6	2.29×10^3
		γ_1	836	0.202	7.1	1.49×10^3
		γ_2	877	0.249	NA	NA
sdH	Bulk	α	32	0.106	12.4	2.65×10^3
	Nanoflake	α	36	0.088	4.2	5.73×10^3
		η_1	1771	0.243	NA	NA
		η_2	1954	0.285	8.9	1.90×10^3
		δ	3929	NA	NA	NA
		α	33	0.094	4.4	5.17×10^3

we find that the oscillation frequency is directly proportional to the extremal cross-sectional areas of the Fermi surface, which are perpendicular to the applied magnetic field. The Fermi surface area (S) is calculated using the Onsager relation [21] $S = 2\pi eF_\alpha/\hbar$, resulting in a value of $3.51 \times 10^{13} \text{ cm}^{-2}$ for the α pocket (37 T), $44.86 \times 10^{13} \text{ cm}^{-2}$ for the β_1 pocket (470 T), $79.79 \times 10^{13} \text{ cm}^{-2}$ for the γ_1 pocket (836 T), $169.03 \times 10^{13} \text{ cm}^{-2}$ for the η_1 pocket (1771 T), and $375.01 \times 10^{13} \text{ cm}^{-2}$ for the δ pocket (3929 T). Unlike GdTe₃ and NdTe₃ [17,19], the temperature dependence of the SdH amplitude in PrTe₃ obeys the L-K formula, suggesting that an interplay

between magnetic ordering and conducting electrons may be lacking.

For the MR measurements, the 60 nm nanodevice exhibited large transverse MR values, reaching up to 1800% at 2 K and 11 T, along with clear sdH oscillations, even at a magnetic field <1000 Oe. The derivative of the MR as a function of $\mu_0 H$ at 2 K is shown in Fig. 3(f), and the corresponding MR data are presented in Fig. 4(a). To determine the carrier mobility in the nanoflake, Hall measurements were conducted, as shown in Fig. 4(b). At low-magnetic-field regions, a distinct nonlinear behavior was observed, suggesting the presence of

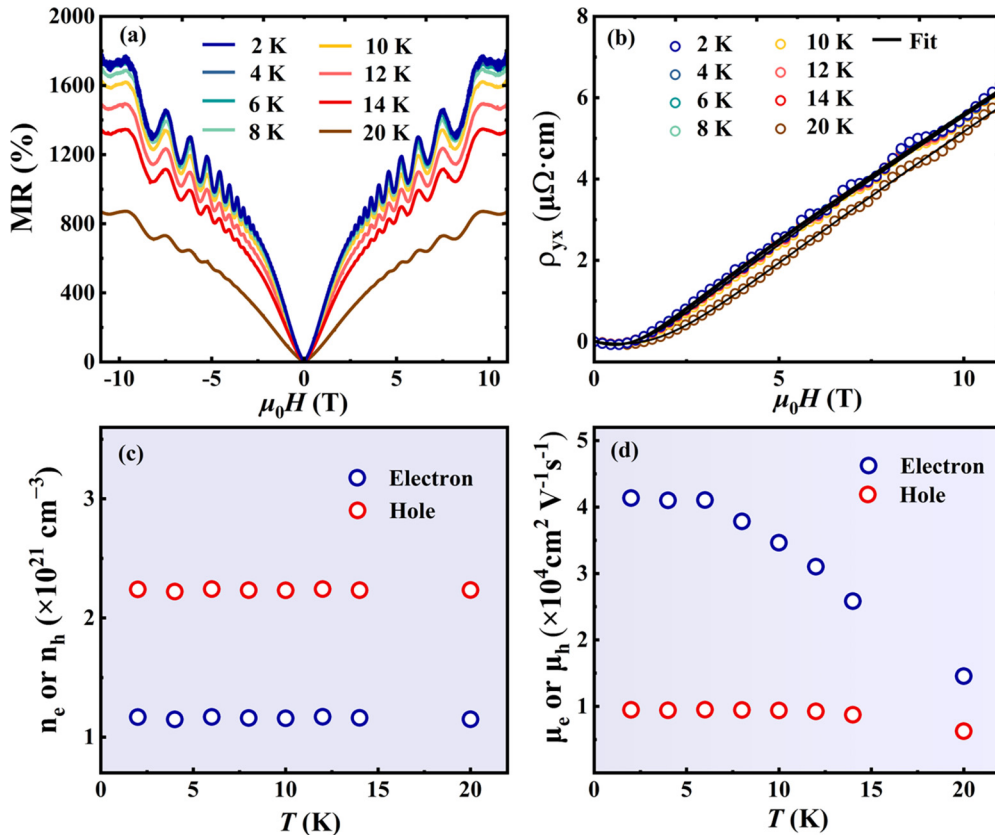


FIG. 4. (a) Magnetoresistance of a 60 nm nanoflake sample measured at various temperatures. (b) Field dependence of Hall resistivity at different temperatures. The black lines represent two band model fits. (c) Temperature-dependent carrier concentrations extracted via two-band model fitting. (d) Temperature-dependent carrier mobilities derived from two-band model fitting.

multiple types of charge carriers contributing to the Hall resistance. Conversely, at high-magnetic-field regions, the Hall resistance profile clearly indicates that hole carriers are the dominant species. This phenomenon can be attributed to the ionic configuration of PrTe_3 , where Pr^{3+} cations are coordinated with $\text{Te}(1)^{2-}\text{Te}(2)^{0.5-}\text{Te}(3)^{0.5-}$ anions, leading to the generation of hole carriers primarily within the $\text{Te}(2)$ - $\text{Te}(3)$ sheets. Remarkably, the Hall resistivity also exhibited oscillations in the high-field region, indicating the high device quality with minimal influence from scattering centers. In our analysis, a two-band model was utilized to accurately fit the ρ_{yx} data, enabling the extraction of carrier mobilities (μ_e and μ_h) and carrier concentrations (n_e and n_h) for both electrons and holes. The underlying model is described below:

$$\rho_{yx}(B) = \frac{B}{e} \frac{(n_h\mu_h^2 - n_e\mu_e^2) + (n_h - n_e)(\mu_e\mu_h B)^2}{(n_h\mu_h + n_e\mu_e)^2 + (n_h - n_e)^2(\mu_e\mu_h B)^2}, \quad (4)$$

$$\rho_{xx}(0) = \frac{1}{e} \frac{1}{n_h\mu_h + n_e\mu_e}, \quad (5)$$

$$\left. \frac{d\rho_{yx}}{dB} \right|_{B \text{ is large}} = \frac{1}{(n_h - n_e)e}, \quad (6)$$

$$\left. \frac{d\rho_{yx}}{dB} \right|_{B=0} = \frac{(n_h\mu_h^2 - n_e\mu_e^2)}{(n_h\mu_h + n_e\mu_e)^2} \cdot \frac{1}{e}. \quad (7)$$

Here, B is the magnetic field, e is the elementary charge, n_e and μ_e are the electron carrier concentrations and mobilities, and n_h and μ_h are the hole carrier concentrations and mobilities, respectively. Through the fitting of Eq. (4) under the conditions outlined in Eqs. (5)–(7), we have derived valuable insights into the carrier concentrations and mobilities. As summarized in Figs. 4(c) and 4(d) for the 60 nm nanoflake, the electron and hole concentrations (n_e and n_h) were evaluated to be 1.17×10^{21} and $2.24 \times 10^{21} \text{ cm}^{-3}$, respectively. Furthermore, the electron and hole mobilities (μ_e and μ_h) were evaluated to be $41\,360$ and $9484 \text{ cm}^2 \text{ V}^{-1} \text{ s}^{-1}$, respectively. Additionally, we extended our investigation to a 120 nm PrTe_3 nanoflake, with corresponding MR and Hall measurements presented in Figs. S5(a) and S5(b) in the Supplemental Material [28]. Utilizing the two-band model, we

unveiled the mobility and carrier concentrations, as illustrated in Figs. S5(c) and S5(d) in the Supplemental Material [28], respectively.

IV. CONCLUSIONS

In this paper, we present a comprehensive investigation of the quantum oscillations and electron structure in single-crystal PrTe_3 through systematic measurements of low-temperature magnetism and magnetotransport properties. By analyzing the AMR and SdH oscillations, we confirm the 2D nature of the Fermi surface, underscoring the importance of its low-dimensional electronic structure. Leveraging the Lifshitz-Onsager quantization rule, a zero Berry phase was revealed in the Landau index against $1/B$, indicating a trivial topology band structure of PrTe_3 . Moreover, our thorough investigation includes a detailed examination of the Hall effect using a two-band model, revealing a remarkably high carrier mobility of $4.1 \times 10^4 \text{ cm}^2 \text{ V}^{-1} \text{ s}^{-1}$ in a 60 nm device. This exceptional mobility underscores the potential of PrTe_3 as a promising candidate for the development of 2D high-mobility devices, paving the way for exciting advancements in the field of electronic materials. In this paper, we contribute to a deeper understanding of the quantum phenomena and transport properties in PrTe_3 , offering valuable insights for future research and technological applications.

ACKNOWLEDGMENTS

We thank Qiang Hou for the helpful discussions. L.L. acknowledges support from the National Natural Science Foundation of China (Grants No. 12204096 and No. 52130706), the Natural Science Foundation of Jiangsu Province (Grant No. BK20220797), and the Fundamental Research Funds for the Central Universities. This paper is also supported by the Open Research Fund Program of the State Key Laboratory of Low-Dimensional Quantum Physics (Grant No. KF202203) and the open research fund of Key Laboratory of Quantum Materials and Devices (Southeast University), Ministry of Education.

-
- [1] W. Kohn, Image of the Fermi surface in the vibration spectrum of a metal, *Phys. Rev. Lett.* **2**, 393 (1959).
- [2] M. H. Whangbo and E. Canadell, Analogies between the concepts of molecular chemistry and solid-state physics concerning structural instabilities. Electronic origin of the structural modulations in layered transition metal dichalcogenides, *J. Am. Chem. Soc.* **114**, 9587 (1992).
- [3] S. Manzeli, D. Ovchinnikov, D. Pasquier, O. V. Yazyev, and A. Kis, 2D transition metal dichalcogenides, *Nat. Rev. Mater.* **2**, 17033 (2017).
- [4] T. L. Adelman, J. McCarten, M. P. Maher, D. A. DiCarlo, and R. E. Thorne, Low-temperature charge-density-wave dynamics and switching in NbSe_3 , *Phys. Rev. B* **47**, 4033 (1993).
- [5] M. H. Lee, C. H. Chen, M.-W. Chu, C. S. Lue, and Y. K. Kuo, Electronically phase-separated charge-density waves in $\text{Lu}_2\text{Ir}_3\text{Si}_5$, *Phys. Rev. B* **83**, 155121 (2011).
- [6] C. S. Snow, J. F. Karpus, S. L. Cooper, T. E. Kidd, and T.-C. Chiang, Quantum melting of the charge-density-wave state in $1T\text{-TiSe}_2$, *Phys. Rev. Lett.* **91**, 136402 (2003).
- [7] J. Joshi, H. M. Hill, S. Chowdhury, C. D. Malliakas, F. Tavazza, U. Chatterjee, A. R. Hight Walker, and P. M. Vora, Short-range charge density wave order in $2H\text{-TaS}_2$, *Phys. Rev. B* **99**, 245144 (2019).
- [8] S. Wang, X. Chen, C. An, Y. Zhou, M. Zhang, Y. Zhou, Y. Han, and Z. Yang, Observation of room-temperature amplitude mode in quasi-one-dimensional charge-density-wave material CuTe , *Appl. Phys. Lett.* **120**, 151902 (2022).
- [9] Y. Chen, P. Wang, M. Wu, J. Ma, S. Wen, X. Wu, G. Li, Y. Zhao, K. Wang, L. Zhang *et al.*, Raman spectra and dimensional effect on the charge density wave transition in GdTe_3 , *Appl. Phys. Lett.* **115**, 151905 (2019).

- [10] N. Ru, J.-H. Chu, and I. R. Fisher, Magnetic properties of the charge density wave compounds $R\text{Te}_3$ ($R = \text{Y, La, Ce, Pr, Nd, Sm, Gd, Tb, Dy, Ho, Er, and Tm}$), *Phys. Rev. B* **78**, 012410 (2008).
- [11] M. Watanabe, S. Lee, T. Asano, T. Ibe, M. Tokuda, H. Taniguchi, D. Ueta, Y. Okada, K. Kobayashi, and Y. Niimi, Quantum oscillations with magnetic hysteresis observed in CeTe_3 Thin Films, *Appl. Phys. Lett* **117**, 072403 (2020).
- [12] J. J. Hamlin, D. A. Zocco, T. A. Sayles, M. B. Maple, J.-H. Chu, and I. R. Fisher, Pressure-induced superconducting phase in the charge-density-wave compound terbium tritelluride, *Phys. Rev. Lett.* **102**, 177002 (2009).
- [13] D. A. Zocco, J. J. Hamlin, K. Grube, J.-H. Chu, H.-H. Kuo, I. R. Fisher, and M. B. Maple, Pressure dependence of the charge-density-wave and superconducting states in GdTe_3 , DyTe_3 , and DyTe_3 , *Phys. Rev. B* **91**, 205114 (2015).
- [14] A. A. Sinchenko, P. Lejay, O. Leynaud, and P. Monceau, Dynamical properties of bidirectional charge-density waves in ErTe_3 , *Phys. Rev. B* **93**, 235141 (2016).
- [15] N. Ru, R. A. Borzi, A. Rost, A. P. Mackenzie, J. Laverock, S. B. Dugdale, and I. R. Fisher, de Haas–van Alphen oscillations in the charge density wave compound lanthanum tritelluride LaTe_3 , *Phys. Rev. B* **78**, 045123 (2008).
- [16] A. A. Sinchenko, P. D. Grigoriev, P. Lejay, and P. Monceau, Spontaneous breaking of isotropy observed in the electronic transport of rare-earth tritellurides, *Phys. Rev. Lett.* **112**, 036601 (2014).
- [17] S. Lei, J. Lin, Y. Jia, M. Gray, A. Topp, G. Farahi, S. Klemenzl, T. Gao, F. Rodolakis, J. L. McChesney *et al.*, High mobility in a van der Waals layered antiferromagnetic metal, *Sci. Adv.* **6**, eaay6407 (2020).
- [18] A. Pariari, S. Koley, S. Roy, R. Singha, M. S. Laad, A. Taraphder, and P. Mandal, Interplay between charge density wave order and magnetic field in the nonmagnetic rare-earth tritelluride LaTe_3 , *Phys. Rev. B* **104**, 155147 (2021).
- [19] K. J. Dalgaard, S. Lei, S. Wiedmann, M. Bremholm, and L. M. Schoop, Anomalous Shubnikov–de Haas quantum oscillations in rare-earth tritelluride NdTe_3 , *Phys. Rev. B* **102**, 245109 (2020).
- [20] E. DiMasi, M. C. Aronson, J. F. Mansfield, B. Foran, and S. Lee, Chemical pressure and charge-density waves in rare-earth tritellurides, *Phys. Rev. B* **52**, 14516 (1995).
- [21] K. Yumigeta, Y. Qin, H. Li, M. Blei, Y. Attarde, C. Kopas, and S. Tongay, Advances in rare-earth tritelluride quantum materials: Structure, properties, and synthesis, *Adv. Sci.* **8**, 2004762 (2021).
- [22] A. Kogar, A. Zong, P. E. Dolgirev, X. Shen, J. Straquadine, Y. Bie, X. Wang, T. Rohwer, I. C. Tung, Y. Yang *et al.*, Light-induced charge density wave in LaTe_3 , *Nat. Phys.* **16**, 159 (2020).
- [23] L. J. Li, E. C. T. O’Farrell, K. P. Loh, G. Eda, B. Özyilmaz, and A. H. Castro Neto, Controlling many-body states by the electric-field effect in a two-dimensional material, *Nature (London)* **529**, 185 (2016).
- [24] A. Chikina, H. Lund, M. Bianchi, D. Curcio, K. J. Dalgaard, M. Bremholm, S. Lei, R. Singha, L. M. Schoop, and P. Hofmann, Charge density wave generated fermi surfaces in NdTe_3 , *Phys. Rev. B* **107**, L161103 (2023).
- [25] L. Nie, K. Sun, W. Ma, D. Song, L. Zheng, Z. Liang, P. Wu, F. Yu, J. Li, M. Shan *et al.*, Charge-density-wave-driven electronic nematicity in a kagome superconductor, *Nature (London)* **604**, 59 (2022).
- [26] E. Lee, D. H. Kim, H. W. Kim, J. D. Denlinger, H. Kim, J. Kim, K. Kim, B. I. Min, B. H. Min, Y. S. Kwon *et al.*, The 7×1 Fermi surface reconstruction in a two-dimensional f -electron charge density wave system: PrTe_3 , *Sci. Rep.* **6**, 30318 (2016).
- [27] S. Seong, H. Kim, K. Kim, B. I. Min, Y. S. Kwon, S. W. Han, B.-G. Park, R. Stania, Y. Seo, and J.-S. Kang, Angle-resolved photoemission spectroscopy study of a system with a double charge density wave transition: ErTe_3 , *Phys. Rev. B* **104**, 195153 (2021).
- [28] See Supplemental Material at <http://link.aps.org/supplemental/10.1103/PhysRevB.109.035121> for further information on the additional magnetization and transport data.
- [29] F. J. Pomiro, J. P. Gaviría, G. G. Fouga, L. D. Vega, and A. E. Bohé, Chlorination of Pr_2O_3 and Pr_6O_{11} . Crystal structure, magnetic and spectroscopic properties of praseodymium oxychloride, *J. Alloy Compd.* **776**, 919 (2019).
- [30] J. Liu, V. Smetana, K. A. Gschneidner Jr., G. J. Miller, and V. K. Pecharsky, The crystal structure and magnetic properties of $\text{Pr}_{117}\text{Co}_{56.7}\text{Ge}_{112}$, *J. Appl. Phys.* **113**, 17E120 (2013).
- [31] F. Wu, C. Y. Guo, M. Smidman, J. L. Zhang, and H. Q. Yuan, Large magnetoresistance and Fermi surface topology of PrSb , *Phys. Rev. B* **96**, 125122 (2017).
- [32] M. Toda, H. Sugawara, K. Magishi, T. Saito, K. Koyama, Y. Aoki, and H. Sato, Electrical, magnetic and NMR studies of Ge-based filled skutterudites $R\text{Pt}_4\text{Ge}_{12}$ ($R = \text{La, Ce, Pr, Nd}$), *J. Phys. Soc. Jpn.* **77**, 124702 (2008).
- [33] K. Takegahara, H. Harima, and A. Yanase, Crystal electric fields for cubic point groups, *J. Phys. Soc. Jpn.* **70**, 1190 (2001).
- [34] G. P. Mikitik and Yu. V. Sharlai, Manifestation of Berry’s phase in metal physics, *Phys. Rev. Lett.* **82**, 2147 (1999).